The phase separation in a rectangular microchannel by micro-membrane

Jinliang Xu [*], Bin An, Dongliang Sun [*]

The Beijing Key Laboratory of Multiphase Flow and Heat Transfer, North China Electric Power University, Beijing, 102206 Beijing, PR China

ABSTRACT

A phase separator was formed by populating an enclosed micro-membrane at the microchannel center. When a bubble train in the bare duct interacted with the micro-membrane, a single bubble was separated into two daughter bubbles to flow in the two side regions. The separated bubbles never entered the micro-membrane inside due to the increased surfaced energy. A multiscale numerical scheme using the Volume of Fluid (VOF) method tracked the gas–liquid interface. The results identified that the separator consisted of a phase separating section and a fully phase separation section. Within the separating section, the two side regions contained confined bubble train flow. The liquid plugs were gradually shortened along the flow direction, caused by liquid flowing towards the micro-membrane inside. Liquid circulations were observed within liquid plugs. The gas–liquid could be fully separated. Within the fully phase separation section, gas was flowing in the side regions, with ultra-thin liquid films on solid walls. The separator had the potential to be used as a condenser. The heat transfer enhancement is related to A_r (the bubble project area relative to the bottom surface area) and an averaged liquid film thickness. In contrast to the bare duct section, the fully phase separation section significantly increased A_r and decreased liquid film thicknesses. The heat transfer intensity in the fully separated flow section can be ten times of that in the bare duct section.

© 2014 Elsevier Ltd. All rights reserved.

1. Introduction

Multiphase flow occurs in a wide range of industrial application from macroscale pipes in thermal power plants, renewable thermal energy utilization systems, air-conditioners, various heat exchangers to microscale assemblies in the microelectronic industry and biotechnologies. The miniaturized systems offer a set of advantages such as high surface-to-volume ratios, high heat and mass transfer rates and safety. The phase separation is an important process in many chemical engineering applications, such as reactive processes and thermal separation processes of components. Engineers have to deal with the phase separation in mini or micro/nano scale.

Wiesegger et al. [1] reviewed recent progresses on the phase separation in microsystems. Several techniques such as the T-junction geometry, capillary force and centrifugal force can separate the two-phase mixture. Gupta [2] commented on the non-dimensional parameters involved in two-phase system such as

Reynolds number ($Re = \rho u d/\mu$): the inertia relative to viscous force; the Froude number ($Fr = \rho u^2/\Delta\rho g d$): the inertia relative to gravity; the Bond number ($Bo = \Delta\rho d^2 g/\sigma$): the gravity relative to surface tension force; the capillary number ($Ca = \mu u/\sigma$): the viscous relative to surface tension force; and the Weber number ($We = \rho u^2 d/\sigma$): the inertia relative to the surface tension force. These dimensionless-parameters indicated that as the channel size decreases, the surface tension force becomes more important. Thus, it is convenient to use the capillary force to separate fluids in microsystems, technically.

The phase separation in capillaries or in a capillary network has been investigated by various researches [3–9]. Membranes were used to deal with the phase separation. The gas/liquid interface was stabilized with a membrane during the evaporation process [10]. Different membranes were investigated on the separation factor and the distillate flux rate. Only the feed concentration influenced the separation efficiency.

A membrane combining hydrophilic and hydrophobic materials was used by Kraus & Krewer [11] to separate CO_2 from water/methanol mixtures in microchannels for direct methanol fuel cells. Effects of the temperature, humidity, flow rates and orientation on the separation efficiency were considered. The separation

* Corresponding authors.
  E-mail addresses: xjl@ncepu.edu.cn (J. Xu), dlsun@ncepu.edu.cn (D. Sun).

Nomenclature

a	Core region width (μm)
A_{bubble}	Bubble project area (μm^2)
A_{bottom}	Bottom wall surface corresponding to the bubble (μm^2)
A_r	Dimensionless bubble contact area
b	Width of each side region (μm)
Ca	Capillary number
Co	Courant number
d	Gap between micro-pin-fins (μm)
D	Bare duct width (μm)
D_h	Hydraulic diameter (μm)
E	Surface energy (J)
F_{vol}	Interface-induced volume force vector (N)
Fr	Froude number
h_{lg}	Latent heat of evaporation (J kg^{-1})
H	Bare channel height (μm)
J	Superficial velocity (m s^{-1})
K	The work which pushes the gas bubble moving (J)
k	Heat transfer enhancement ratio
L	Length (μm)
L_{unit}	A unit Taylor bubble length (μm)
$\dot{m}$	Condensation rater per unit wall area (J s^{-1} m^{-2})
$\dot{M}$	Condensation rate (J s^{-1})
P	Integration perimeter over the channel cross section (μm)
Q	Volume flow rate (m^3 s^{-1})
R_{center}	Radius shown in Fig. 4 (μm)
R_{cornor}	Radius shown in Fig. 4 (μm)
Re	Reynolds number
t	Time (ms)

T	Temperature (K)
u	Velocity in x coordinate (m s^{-1})
V	Bubble volume (μm^3)
v	Velocity in y coordinate (m s^{-1})
$\vec{v}$	Velocity vector
w	Micro-pin-fin width (μm)
We	Weber number
x	x coordinate
y	y coordinate
z	coordinate

Greek letters

α	Gas volume flow rate relative to the total volume flow rate
ε	Void fraction
κ	Interface curvature (m^{-1})
μ	Dynamic viscosity (Pa s)
θ	Contact angle
ρ	Density (kg m^{-3})
δ	Liquid film thickness (μm)
σ	Surface tension (N m^{-1})

Subscripts

a	Average
B	Bare duct section
M	Modulated flow section
g	Liquid phase
l	Vapor phase
sat	Saturation
w	Wall

efficiencies could reach 100%. Zenith et al. [12] used the interface tracking method (volume of fluid, called VOF) in Fluent to model the phase separation in a separator that was experimentally studied by Kraus and Krewer [11]. The separator orientation with respect to gravity was found to have small influence on the separator performance. David et al. [13] used a hydrophobic *PTEE* membrane with 220 nm pores to vent the vapor phase from water boiling in microchannels.

Recently, our group proposed the phase separation concept in a meter-scale long condenser tube [14]. A hollow mesh cylinder was suspended in the tube, dividing the tube cross section into an annular region and a core region. The mesh cylinder was made of a piece of stainless mesh screen. Gas bubbles were prevented from entering the mesh cylinder thus they were flowing in the annular region. Liquid, however, could be pushed toward the mesh cylinder inside. The air–water experiment was performed to verify the phase separation effectiveness. Subsequent, Chen et al. [15] performed the numerical simulation of the flow pattern modulation in a long tube. The vertical upflow was considered. The authors used the non-uniform base grid and dynamic grid adaption methods. The VOF method simulated the problem. The simulation results demonstrated the separated flow paths of gas and liquid. The liquid film on the tube wall becomes ultra-thin, that is very helpful for the heat transfer enhancement.

Our proposed heat transfer tube with the phase separation concept is a typical multiscale system, linking the micro scale of mesh pores with the meter-long tube. Besides, the device had circular shape. The objective of this paper is to extend our phase separation technique to the microchannel network. The phase separation was fulfilled in a rectangular microchannel. An enclosed

micro-membrane with open exit was symmetrically located in the rectangular microchannel. The micro-membrane was formed by lined pin-fin array. Thus, the microchannel cross section was divided into a core region formed by the micro-membrane, and two side regions that were close to the two side channel walls. The separation efficiency can be up to 100%, and the liquid film thickness was significantly reduced. Practically, the device can be made by the etching technique. It can be operated with varied flow rates of the two-phases, as long as the pore size between two neighboring pin-fins is small enough.
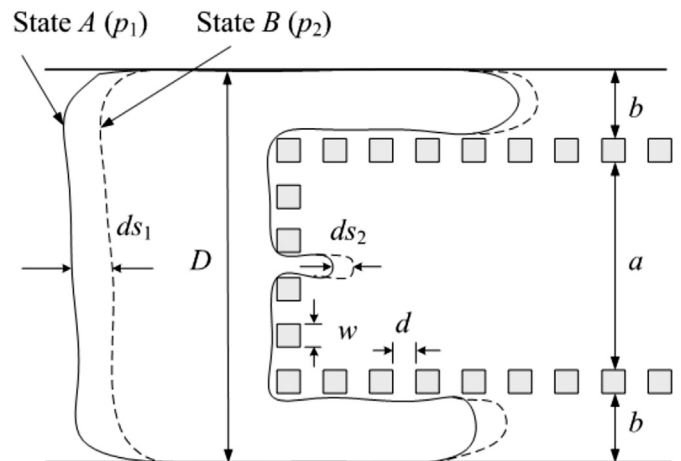

Fig. 1. The phase separator with an enclosed micro-membrane with an open exit.

2. The phase separation by capillary force

Fig. 1 shows the separator with the micro-membrane structure in a rectangular duct. A set of micro-pin-fins were lined to form an enclosed micro-membrane with an open exit. Thus, the cross section was divided into a core region and two side regions close to the side duct walls. The gap between two neighboring pin-fins was d (recorded as the pore diameter). Each of the two side regions had the width of b, and the core region had the width of a (see Fig. 1).

Bubbles are difficult to enter the core region if d is sufficiently small. This is because the surface energy of gas bubble should be increased when the bubble interface moves from a larger space into a smaller space. Considering a large bubble with its width identical to the duct width D is penetrating the pore with its size d, the surface energy of the gas bubble between state A (initial state) and B (ending state) is

$$dE = 2\sigma(d + H)ds_2 - 2\sigma(D + H)ds_1 \tag{1}$$

where E is the surface energy, σ is the surface tension, d is the gap of the micro-pin-fins, D and H are the channel width and depth, respectively, ds_1 is the moving distance from state A to state B in the bare duct, ds_2 is the distance penetration the micro-pore (see Fig. 1). The mass conservation for the gas bubble yields

$$dHds_2 = DHds_1 \tag{2}$$

Thus the work required to transform the gas bubble from state A to B is.

$$dK = p_1DHds_1 - p_2dHds_2 \tag{3}$$

where K is the work, p_1 and p_2 are the gas bubble pressures at the state A and B, respectively. The p_1 and p_2 had the following relationship with $dK = dE$.

$$p_1 - p_2 = 2\sigma\left(\frac{1}{d} - \frac{1}{D}\right) \tag{4}$$

Equation (4) illustrates that the second term of the right side of Eq. (4) contributes less to the pressure difference due to $D \gg d$. Giving $\sigma = 0.07275$ N/m for an air–water system at 20 °C and $d = 5$ μm, p_1-$p_2 = 29$ kPa, indicating a pressure difference of about 30 KPa required to penetrate a bubble interface within the micropores.

Similarly, if a bubble is penetrating from a side region to a micropore, the pressure difference can be deduced as [16]:

$$p_1 - p_2 = 2\sigma\left(\frac{1}{d} - \frac{1}{b}\right) \tag{5}$$

A large pressure difference of $p_1 - p_2$ can be obtained if d is significantly smaller than b.

3. The configuration and problem statement

Fig. 2a shows the designed microfluidic network (planar view), which consisted of three parts: an upstream bubble generator part, a middle bare duct part, and a downstream separated flow part. Initially, the two side branch ducts were arranged perpendicular to the axial flow direction. Air and water entered the air inlet 1 and the two side branch duct 2, respectively. The Taylor bubbles could be consecutively generated by the T-junction geometry.

The middle bare duct was long enough to reach a fully developed bubble train flow. The bubble dynamics and flow field were compared with those in the downstream separated flow part. An enclosed micro-membrane with an open exit was located symmetrically in the rectangular duct. The open exit was used to discharge fluids. The micro-membrane was formed by the micro-pin-fin structure.
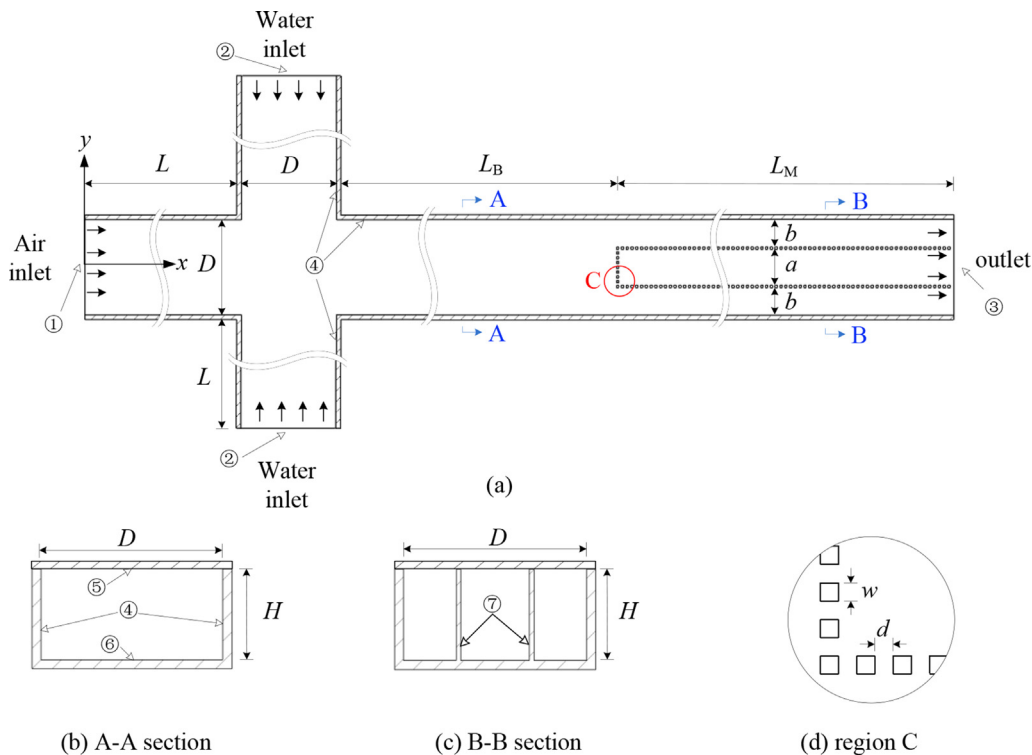

(a)

(b) A-A section   (c) B-B section   (d) region C

Fig. 2. The microchannel structure. (a) top view; (b) A–A cross section; (c) B–B cross section; (d) enlarged micro-membrane corner (① air inlet; ② water inlet; ③outlet; ④ side wall; ⑤ adiabatic cover wall; ⑥ bottom wall; ⑦ micro-pin-fin).

Fig. 2 shows the major dimensions. The rectangular duct width and depth were D and H, respectively. The air inlet and two water inlets had the same length L. The bare duct and the separated flow part had the length of L_B and L_M, respectively. The micro-pin-fin had the square cross section with the width of w. The gap between two neighboring pin-fins was d. The two side regions had the gap width of b and the core region had the width of a. Table 1 shows the major dimensions used in this study, having $D = 200$ μm, $H = 100$ μm, $a = 115$ μm, $b = 37.5$ μm, $w = 5$ μm and $d = 5$ μm. Because the microfluidic device had the potential to be used as an efficient condenser, the top wall (surface 5) was assumed to be adiabatic. But the two side surface 4 and bottom surface 6 had the same wall temperatures (see Fig. 2b). The pin-fin surface was called surface 7 (see Fig. 2c). The three-dimensional coordinates of x, y and z were marked in Fig. 2.

The air inlet had the uniform inlet velocity of u_{in}. Based on the definition, the superficial air velocity of J_g in the two-phase part L_B equals to u_{in}. The two side branch duct had the uniform water velocity of u_w. Thus, the superficial water velocity was $J_l = 2u_w$. The two-phase Reynolds numbers were defined based on the superficial velocities of the two-phases:

$$Re_l = \frac{\rho_l J_l D_h}{\mu_l}, \quad Re_g = \frac{\rho_g J_g D_h}{\mu_g} \tag{6}$$

where subscripts of l and g represented the liquid and gas phases, respectively. D_h is the hydraulic diameter:

$$D_h = \frac{4DH}{2(D + H)} \tag{7}$$

here D_h is 133 μm.

4. Numerical method and solution procedure

4.1. Governing equations

The interface capturing and tracking method is suitable for multiphase flow in which the interface can be explicitly captured, for example when the interface is larger than the grid size [2]. Only a single set of conservation equations are solved and the interface is tracked using an additional advection equation. The bulk properties of the fluid in these equations are the volume fraction weighted average of the properties of the two fluids. An additional equation for the gas void fraction is solved to identify the interface location. The governing equations (Volume-of-Fluid, called VOF) are as follows:

The advection equation of the volume fraction:

$$\frac{\partial \alpha}{\partial t} + \overrightarrow{v} \cdot \nabla \alpha = 0 \tag{8}$$

The continuity equation:

$$\nabla \cdot \overrightarrow{v} = 0 \tag{9}$$

The momentum equation:

$$\frac{\partial}{\partial t}(\rho \overrightarrow{v}) + \nabla \cdot (\rho \overrightarrow{v} \overrightarrow{v}) = -\nabla p + \nabla \cdot \left[\mu\left(\nabla \overrightarrow{v} + \nabla \overrightarrow{v}^T\right)\right] + \overrightarrow{F_{vol}} \tag{10}$$

in which

$$\rho = \rho_l \alpha_l + \rho_g \alpha_g \tag{11}$$

$$\mu = \mu_l \alpha_l + \mu_g \alpha_g \tag{12}$$

Table 1
Parameters of the microchannel (μm).

L	800	a	115
L_M	4000	b	37.5
L_B	8000	w	5
D	200	d	5
H	100		

In Eqs.(8)–(12), α is the void fraction, t is the time, $\overrightarrow{v}$ is the velocity vector, ρ and μ are the density and viscosity respectively. The volume force due to the surface tension effect in Eq. (10) is modeled as [17]:

$$F_{vol} = \sigma \frac{\alpha_l \rho_l \kappa_l \nabla \alpha_l + \alpha_g \rho_g \kappa_g \nabla \alpha_g}{0.5(\rho_l + \rho_g)} \tag{13}$$

where σ is the surface tension, κ is the interface curvature having the following expression:

$$\kappa_l = -\kappa_g = -\nabla \cdot \left(\frac{\nabla \alpha_l}{|\nabla \alpha_l|}\right) \tag{14}$$

The contact angle of the fluid contacted with the wall adjusts the surface normal in cells near the wall, resulting in the curvature adjustment of the surface near the wall. If the contact angle is recorded as θ, the surface normal at the live cell next to the wall is:

$$\hat{n} = \hat{n}_w \cos \theta + \hat{t}_w \sin \theta \tag{15}$$

where $\hat{n}_w$ and $\hat{t}_w$ are the unit vectors normal and tangent to the wall, respectively. The contact angle is only important when both of the phases contact with the solid wall or the liquid film around the gas bubble is so thin that the van der Waal forces act across the film. Once a slug bubble is formed with a liquid film on the wall, wall adhesion plays no role to decide the bubble shape. This treatment is similar to that of Mehdizadeh et al. [18].

4.2. The grid generation and interface tracking

The rectangular channel had the cross section of 200 μm × 100 μm. Each micro-pin-fin had the cross section of 5 μm × 5 μm. In order to successfully perform the numerical simulation, a multiscale grid system was used. For the two side branch ducts and the bare duct, a uniform grid size of 8 μm was applied along the flow section. In the modulated flow region, a grid size of 1.25 μm was used. The two grid sizes were adapted with each other using the adaptor ratio of 5:1. The first layer of the grid near the solid wall surface was 50 nm. Fig. 3 shows the generated grid system, including the grids near the micro-pin-fin region and the corner region. The sensitivity analysis of the grid number on the flow was performed. It was found that further refinement of grids had no influence on the flow behavior.

4.3. Differencing schemes

The finite volume method (FLUENT version 6.3.26) solved Eqs.(8)–(10) and boundary conditions. The second order upwind scheme was applied for momentum discretization and the SIMPLE algorithm dealt with the pressure–velocity coupling. The geometric reconstruction scheme captured the interfaces accurately. The time marching of the continuity and momentum equations was fulfilled by the first-order implicit scheme. The time step is controlled by the Courant number, written as
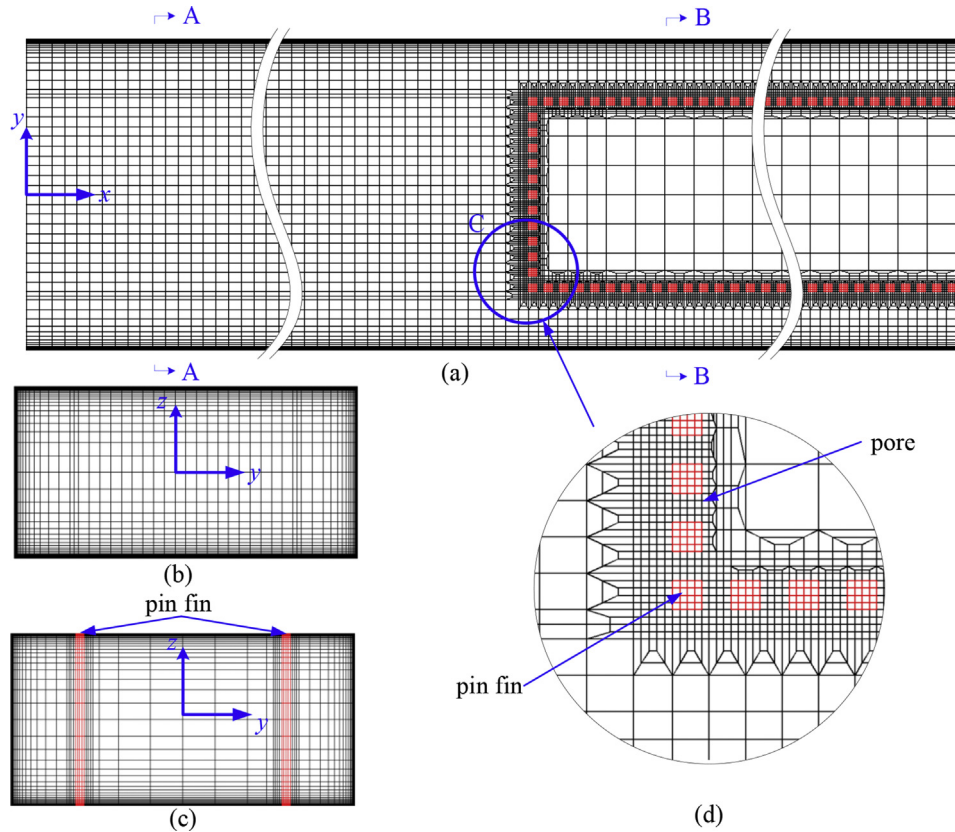
$$Co = \frac{\Delta t}{\Delta x / v} \tag{16}$$

Fig. 3. The multiscale grids for the phase separator (a) top view; (b) A–A cross section; (c) B–B cross section; (d) enlarged micro-membrane corner.

where Δx is the grid size and v is the fluid velocity. The Courant number was set to 0.25 in this study.

5. Results and discussion

5.1. The verification of this simulation

Before our presentation for the separated flow, the numerical simulation was performed for air–water slug flow in a square microchannel, having a channel width of 200 μm and a length of 10 mm. The Taylor bubble with its length of 600 μm was arranged following the tube entrance of 0.5 mm. The water inlet velocities were 1 m/s, 2 m/s and 4 m/s, corresponding to the capillary number

of 0.01646, 0.03647 and 0.07899, respectively. Fig. 4 shows the comparison between our simulations with those of Hazel & Heil [19] and Shikaono & Han [20], in which R_{center} and R_{corner} were defined as

$$R_{center} = \frac{D_h - 2\delta_{center}}{D_h} \tag{17}$$

$$R_{corner} = \frac{\sqrt{2}D_h - 2\delta_{corner}}{D_h} \tag{18}$$

where δ_{center} and δ_{corner} were marked in Fig. 4a. It was noted here that the data were obtained at the axial location of 8 mm ($40D_h$)
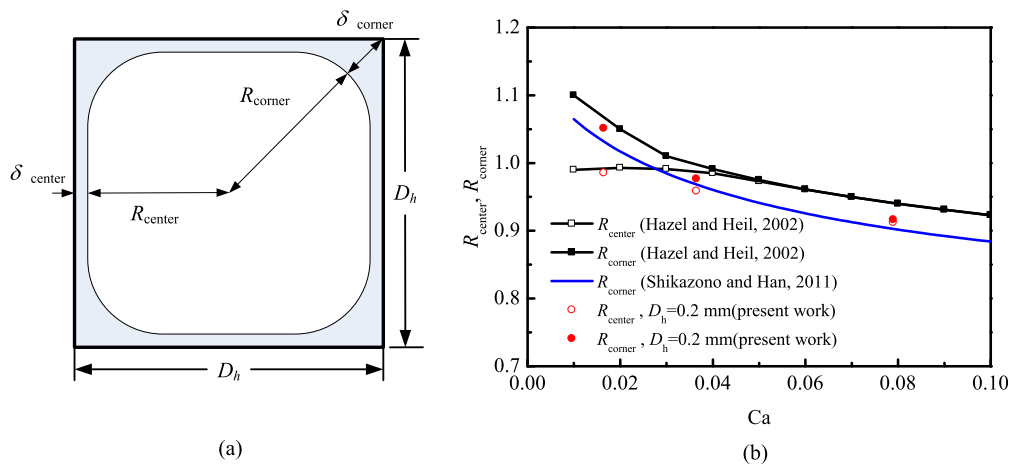

Fig. 4. Dimensionless R_{center} and R_{corner} in a square channel (a) cross section of channel; (b) R_{center} and R_{corner} compared with correlation.

Fig. 4 shows that the capillary number (Ca) influences the bubble shape (R_{corner} relative to R_{center}). The bubble behaved the confined state having $R_{corner} > R_{center}$ for $Ca<0.04$, but the suspended state having $R_{corner} = R_{center}$ for $Ca>0.04$. In summary, the present simulations matched the predictions by Hazel & Heil 2002 with the maximum deviation of 3.6%. The present simulations deviated from the R_{corner} correlation of Shikazono & Han [20] by less than 5%, in which R_{corner} was

$$R_{corner} = 1.171 - \frac{2.43Ca^{2/3}}{1 + 7.28Ca^{2/3} - 0.255We^{0.215}} \quad (\text{Re} < 2000) \tag{19}$$

where We is the Weber number and Ca is the capillary number.

5.2. Run cases

Table 2 shows three cases with same J_l but different J_g. The liquid superficial velocity in the bare duct was 0.669 m/s, corresponding to the liquid superficial Reynolds number of 100 in the bare duct. The J_g in case 2 was arranged so that gas in the two side regions and liquid in the core region had same average velocities, assuming the two-phases can be fully separated in the modulated flow section (see Table 2). Case 1 had smaller but case 3 had larger gas superficial velocities than case 1. Using different J_g was to verify the separator effectiveness.

Table 3 further specified some parameters. The parameter α was defined as the gas volume flow rate relative to the total volume flow rate: $\alpha = Q_g/(Q_g + Q_l)$, where Q_g and Q_l were the volume flow rates of gas and liquid, respectively. Table 3 also gave the void fractions, ε, in the bare duct section and modulated flow section. For ε in the bare duct, it is computed as $\varepsilon = V_g/(AL_{unit})$, where V_g was a bubble volume contained in a single slug bubble unit, A was the cross sectional area of the bare duct and L_{unit} was the bubble unit length. For ε in the fully separated flow section, it was computed over the whole cross section, which equals to $2b/a = 0.32$. All the following figures are for the case 1, except that the mean-averaged liquid film thickness were presented for the three cases in Fig. 11. Table 4 summarized the most important parameters of the phase separator used as a condenser.

5.3. The phase separation process

The bubble movement in the rectangular microchannel was dynamically tracked, in which $t = 0$ was defined as the time at which the first bubble appeared at the T-junction of the microfluidic duct. Fig. 5 shows the pattern in the horizontal duct at $t = 18.8$ ms. Regions A, B, C and D were marked in the figure, in which region A refers to the Taylor bubble in the bare duct, region B refers to the bubble crossing state interacted with the enclosed micro-membrane, region C refers to the merging state in the modulated flow section, and region D refers to the fully separated flow section.

The focused Taylor bubble in region A was 381 μm in length. The liquid plug between two neighboring Taylor bubbles had a length of

Table 2
Operating conditions for three different air–water slug flows.

Case	J_g (m/s)	J_l (m/s)	Re_g	Re_l
1	0.287	0.669	2.456	100
2	0.431	0.669	3.684	100
3	0.574	0.669	4.912	100

Table 3
Void fractions in the bare tube section and modulated flow section.

Case	Homogeneous void fraction $\alpha = J_g/(J_g + J_l)$	Void fraction ε	
		B	M
1	0.30	0.24	0.32
2	0.39	0.30	0.32
3	0.46	0.36	0.32

B and M represents bare duct section and fully phase separation section, respectively.

Table 4
Parameters in the bare duct section and fully phase separation section.

Case	A_r		δ_a (μm)		A_r/δ_a (1/mm)		$\dfrac{(A_r/\delta_a)_M}{(A_r/\delta_a)_B}$
	B	M	B	M	B	M	
1	0.72	1.9	6.34	1.47	0.11	1.29	11.4
2	0.90	1.9	6.64	1.78	0.13	1.07	8.2
3	1.03	1.9	7.25	1.91	0.14	0.99	7

B and M represents the bare duct section and fully phase separation section, respectively.

762 μm. The Taylor bubble consisted of a bubble nose, a bubble body and a bubble tail. The thin liquid film was formed between the Taylor bubble body and the duct wall. The shape of the bubble tail was dependent on the capillary number and it was protruding due to the small capillary number for the air–water system. This shape was consistent well with the analysis reported by Taha & Cui [21]. Due to the large aspect ratio of the duct width to the depth, the bubble was more confined on the duct top and bottom walls than on the two side duct walls (see the bubble shape in Fig. 5a). Three cross sections were marked in Fig. 5a. The thick liquid films were identified in the duct corner, especially over the cross sections of A1 and A2.

Region B shows a bubble interacting with the enclosed micro-membrane. The bubble was separating into two daughter bubbles in the two side ducts. It was found that the bubble did not enter the core region of the duct. The distance between two neighboring micro-pin-fins, d, was small enough so that the surface energy increment for the bubble penetrating into small pores (see Eq. (5)) was larger than the pressure difference across the two sides of the micro-membrane surface. The apparent change of the liquid film thickness was observed in the bubble separating process. The liquid films were significantly thinner in the side ducts than those in the bare duct (see Fig. 5b).

Fig. 5c and d shows confined bubbles in the two side channels, which were merging for the adjacent daughter bubbles in Fig. 5c. The daughter bubbles were fully merged in Fig. 5d. The cross section views are similar in Fig. 5c and d. The core region was full of liquid and the two side regions contained confined gas phase with thin liquid films on the duct walls. Based on the diagram shown in Fig. 5, regions A, B, C and D are called the bare duct section, separating flow section, merging section and fully separated flow section. It was observed that the liquid plugs were gradually shortened in region C until the liquid plugs were shortened to zero at the state of region D. The reason of the shortened liquid plugs was due to the liquid flow from the side channels towards the core channel in region C, which will be verified by the radial velocity distribution in the following figures.

Fig. 6 shows the flow field along various flow sections on the earth coordinate (or called the laboratory coordinate). Fig. 6a shows the four flow sections. Fig. 6b–e shows the flow fields over the horizontal plane at the half height ($z = 0$), in which x_s and x_e stand for the starting location and ending location on the focused area. The flow field at the center between two neighboring bubbles
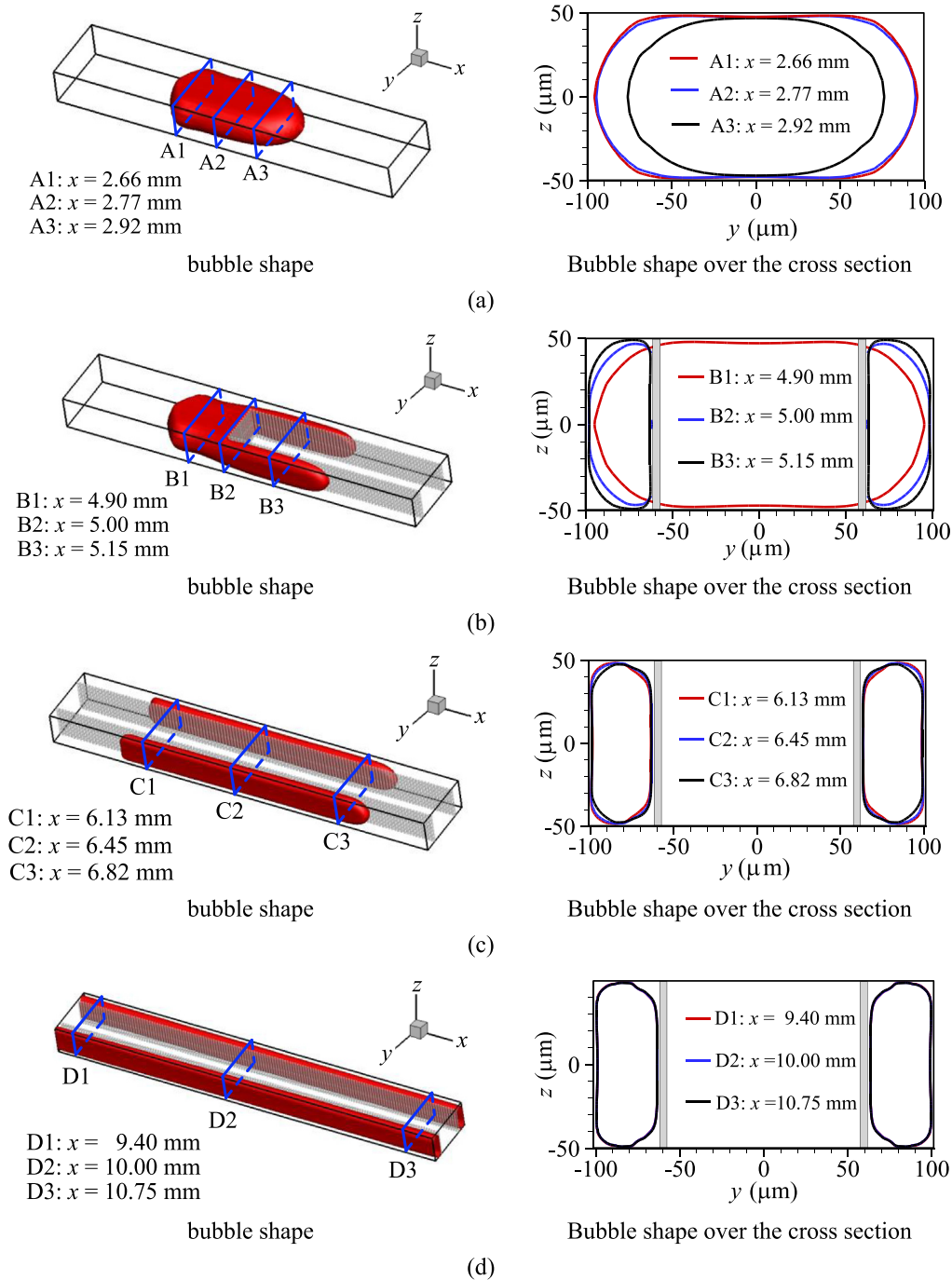
Fig. 5. The phase separation process (case1, $t = 18.8$ ms): (a) region A: $x = 2.45–3.1$ mm; (b) region B: $x = 4.6–5.55$ mm; (c) region C: $x = 5.57–7.1$ mm; (d) region D: $x = 9.35–10.83$ mm.

exhibits the perfect parabola distribution across the duct width. The parabola distribution was slightly deformed when the axial location approaches the bubble nose or bubble tail (see Fig. 6b and c). Fig. 6d shows the segmented confined bubble train in the two side regions and liquid in the core region. The liquid in the core region also exhibits the parabola velocity distribution across channel width. Fig. 6e shows the perfect separated flow situation without segmented liquid plugs in the side regions.

An alternative way to present the flow field uses the reference coordinate, which was attached on the Taylor bubble body (see Fig. 7). Because the flow field was plotted assuming the "stationary"

Taylor bubble, the flow field was significantly different from that shown in Fig. 6. The circulating flow in liquids was apparently observed in the bare duct section (Fig. 7b) and at the micromembrane entrance (Fig. 7c). Besides, the circulating liquid flow was also identified in the two side regions when the daughter bubbles were fully separated from their mother bubble (see Fig. 7d). The liquids had negative axial velocity near the duct walls and positive axial velocities in the duct center. For practical applications, the circulating liquid flows promote the heat and mass transfer for liquid plugs. The circulating flows were also observed by other researchers such as Muzychka et al. [22].
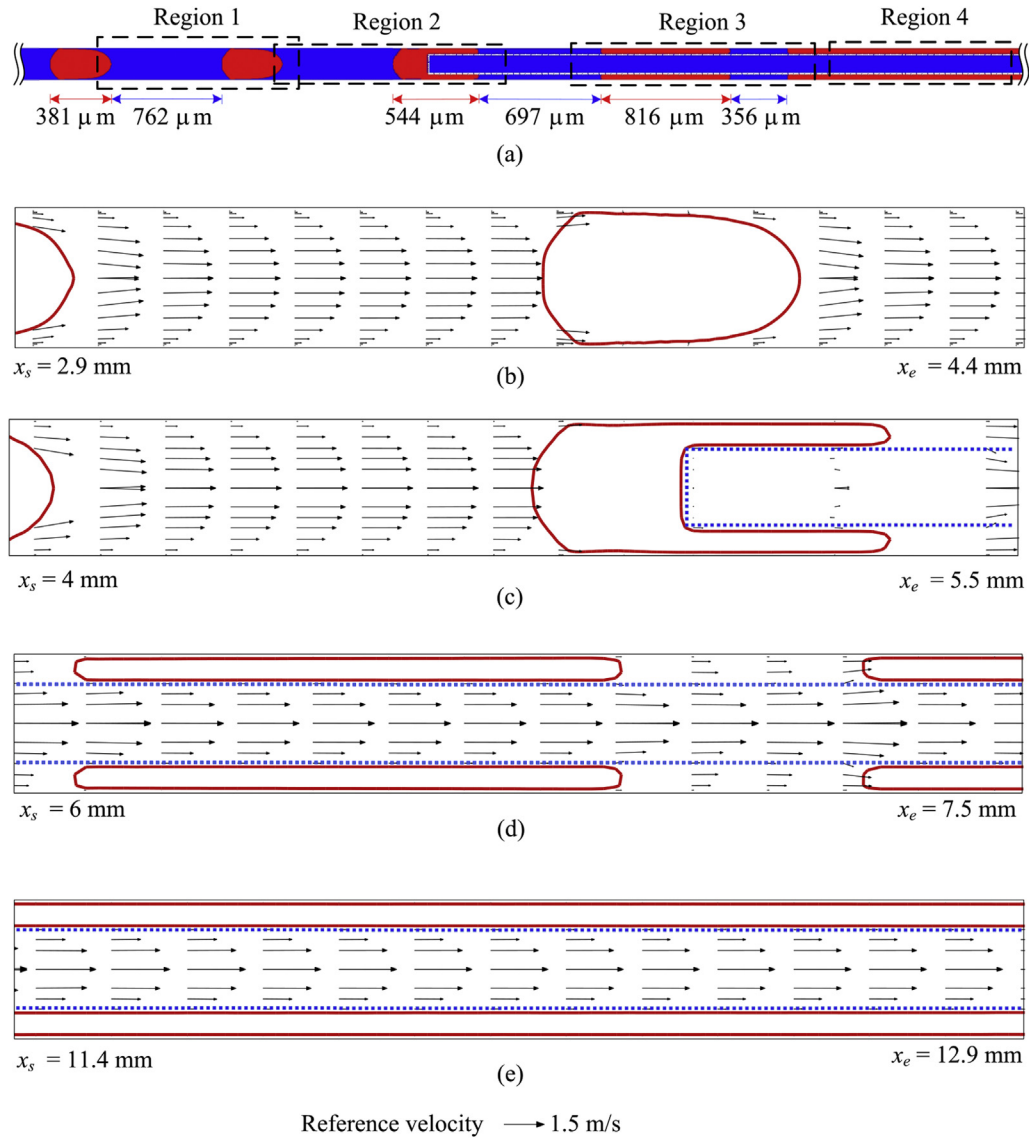
Fig. 6. Bubble shape and velocity field (case1, $t = 18.8$ ms): (a) phase distribution; (b) region A: $x = 2.9$–4.4 mm; (c) region B: $x = 4.0$–5.5 mm; (d) region C: $x = 6.0$–7.5 mm; (e) region D: $x = 11.4$–12.9 mm.

The circulating flow was stopped when the daughter bubbles were fully merged. Instead, the co-current flow was established for the gas core and liquid films on the duct wall. Fig. 7e shows the axial velocity profile within the liquid film on the duct wall. The velocity was absolutely zero on the wall and exhibits the linear distribution within the liquid film. The axial velocity at the gas–liquid interface was 3.78 mm/s (see Fig. 7e).

The bubble velocity was tracked along the whole flow section (see Fig. 8). An average velocity was defined as $u_a = (Q_g + Q_l)/A$, where Q_g and Q_l are the volume flow rates of the gas and liquid phases, A is the cross sectional area of the bare duct. The velocity of u_a was 0.96 m/s for case 1. The Taylor bubble had a uniform velocity of 1.17 m/s in the bare duct section. However, the bubble was accelerating in the separating process. The bubble velocity was sharply increased to 1.81 m/s at $x = 5.0$ mm (the start location of the micro-membrane) and then reduced. The velocity of the gas phase was finally stabilized to 1.13 m/s, which was consistent with the value of $Q_g/(2bH)$, where b and H are the side duct width and height, respectively.

The cross sectional flow field and the near-pore flow field were examined to explain the fully separated flow phenomenon (see Fig. 9). Fig. 9a shows the radial velocity, v, versus the axial flow direction. Bubbles 1 and 2 are the segmented bubbles. Beyond the bubble 3 was the fully separated flow section. The positive radial velocity means the flow from the core region to the side region. Alternatively, the negative value means the flow from the side region to the core region. When the micro-membrane was covered by the gas bubble, the radial velocity was zero to indicate no any mass transfer across the micro-membrane surface, under which the micro-pores were "blocked" by the bubble interface. However, the radial velocities were not zero when the micro-membrane surface was flushed by the liquid plug between two neighboring daughter bubbles. The significantly negative radial velocities dominated over the most liquid plug length. Small positive radial velocities only appeared within a short length at each bubble tail. For instance, the negative radial velocity reached about −1.04 m/s at the front of bubbles 1 and 2. But the positive velocity only reached about 0.18 m/s at the tail of bubbles 2 and 3. The negative radial velocities in liquid plugs caused the gradually shortened liquid plug length along the flow direction. The continuous flow from the side region to the core region was responsible for the fully separated flow
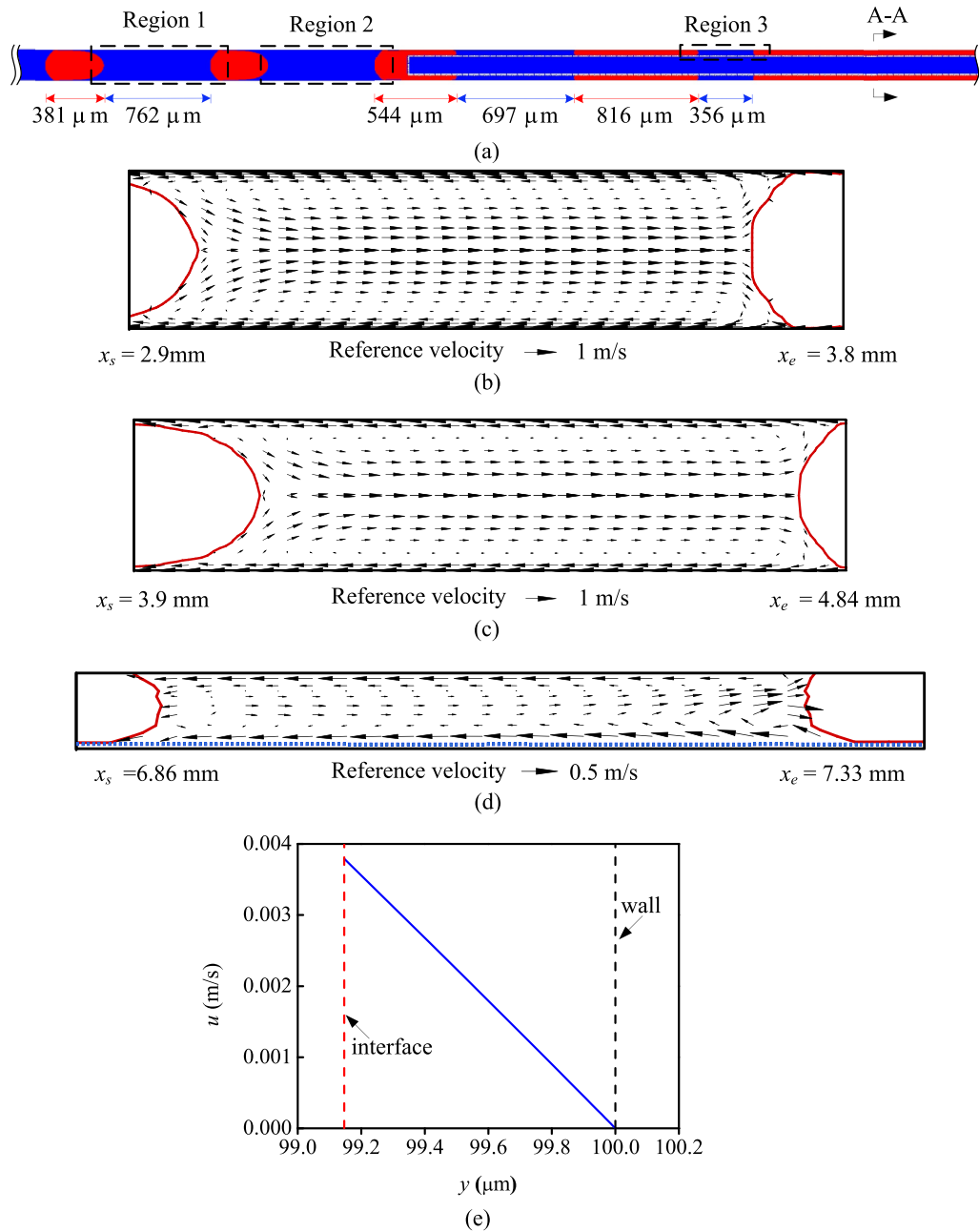
Fig. 7. Bubble shape and relative velocity field: (a) bubble pattern in the whole section; (b) velocity field in region 1; (c) velocity field in region 2; (d) velocity field in region 3; (e) axial velocity in liquid film over the cross Section A—A (case 1, t = 18.8 ms).

condition. Fig. 9a shows the enlarged near-pore flow field at the nose of bubble 1 and the tail of bubble 2, in which four micro-pin-fins were focused on. Large radial flow was observed from the side region to the core region at the bubble nose. Fig. 9b and c shows the flow field at the A—A and B—B cross sections, noting the velocity scales of 1.0 m/s in Fig. 9b and 0.2 m/s in Fig. 9c, respectively.

5.4. A novel micro-condenser design

Figs. 2 and 3 show the phase separator with intermittent flow involved, which can be used as a condenser in microscale. The benefit of using the phase separation concept for condenser applications is the ultra-thin liquid film generated by the device. The top glass cover was assumed to be adiabatic. The bottom

wall and other side walls as well as the pin-fin surfaces were assumed to have the temperature of T_w. This assumption was reasonable because silicon had large thermal conductivity. The liquid—vapor flow had the saturation temperature of T_{sat} in the microstructure. Here we evaluate the condenser heat transfer enhancement using the data of air—water flow reached in the above section. The analysis was based on the fact that the condensation heat transfer at the liquid—vapor interface is much stronger than the liquid heat transfer within the liquid plugs for intermittent flow. A general vapor condensation rate M (kg/s) was developed. Then the parameter with the fully phase separated part relative to the bare duct part was obtained for such evaluation. The vapor condensation rate over the bubble project area A_{bubble} was
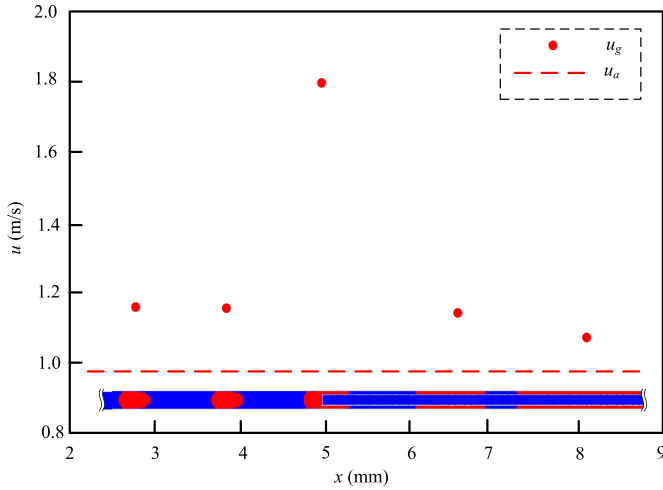
Fig. 8. Bubble velocities along the flow direction (case 1, $t = 18.8$ ms).

$$\dot{M} = \frac{Q}{h_{lg}} = \frac{1}{h_{lg}} \int_0^{A_{bubble}} \lambda_l \frac{T_{sat} - T_w}{\delta} dA = \frac{\lambda_l(T_{sat} - T_w)}{h_{lg}} \int_0^{A_{bubble}} \frac{1}{\delta} dA \tag{20}$$

here λ_l is the liquid thermal conductivity and h_{lg} is the latent heat of evaporation, δ is the local liquid film thickness. Equation (20) was rewritten as

$$\dot{M} = \frac{\lambda_l(T_{sat} - T_w)}{h_{lg}} \int_0^{A_{bubble}} \frac{1}{\delta} dA = \frac{\lambda_l(T_{sat} - T_w)A_{bubble}}{h_{lg}} \frac{\int_0^{A_{bubble}} \frac{1}{\delta} dA}{A_{bubble}} \tag{21}$$

A mean-averaged liquid film thickness over the bubble project area, δ_a, was introduced here:

$$\delta_a = \frac{A_{bubble}}{\int_0^{A_{bubble}} \frac{1}{\delta} dA} = \frac{A_{bubble}}{\int_0^{L_{bubble}} \int_0^P \frac{1}{\delta} dxds} \tag{22}$$

where L_{bubble} is the bubble length, s is the integration coordinate along the duct circumference with heat transfer taking place (not
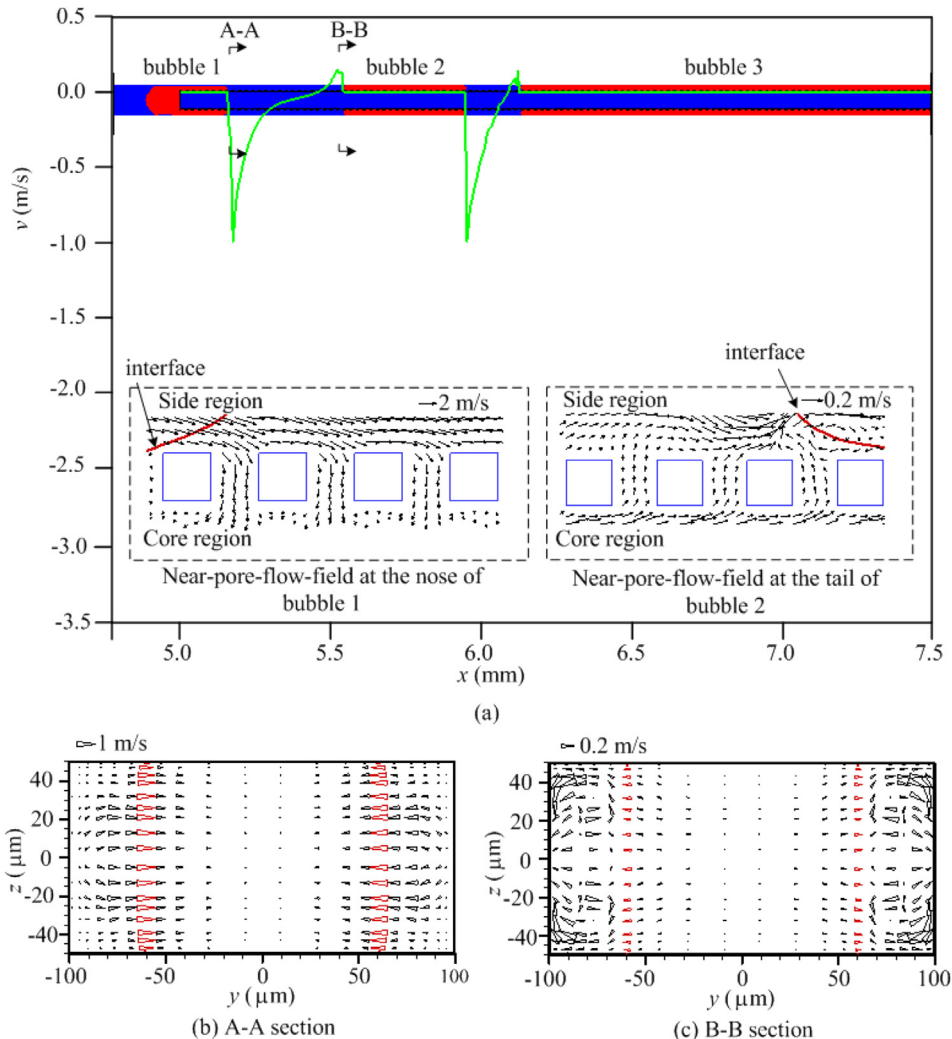

Fig. 9. Radial velocities and near-pore-flow-field (a, case 1, $t = 18.8$ ms), near-pore-flow-field at A–A cross section (b), and near-pore-flow field at B–B cross section (c).

including the top cover width), P is the perimeter. Thus, Eq. (21) was rewritten as

$$\dot{M} = \frac{Q}{h_{lg}} = \frac{\lambda_l(T_{sat} - T_w)}{h_{lg}} \frac{A_{bubble}}{\delta_a} \qquad (23)$$

We computed the condensation rate per bottom surface area, A_{bottom}, as

$$\frac{\dot{M}}{A_{bottom}} = \frac{\lambda_l(T_{sat} - T_w)}{h_{lg}} \frac{A_{bubble}}{A_{bottom}\delta_a} \qquad (24)$$

Fig. 10a shows the phase pattern in the bare duct section and the fully phase separated flow section. Fig. 10b shows a bubble unit having a slug bubble and a liquid plug in the bare duct. The surface A_{bottom} contained a slug bubble and a liquid plug. The surface A_{bubble} referred to the bubble projected area on two side wall surfaces and a bottom surface where the slug bubble was populated. Fig. 10c shows the fully developed phase separation section, noting that the bubble merging region was not considered. The gas and liquid phase were fully separated with gas flowing in two side regions and liquid flowing in the core region. A bottom surface was selected as A_{bottom}. The project area of the gas phase shielded on the side wall, bottom wall (side region) and a set of pin-fin surface (see Fig. 10c).

Equation (24) was rewritten as follows by defining a parameter of $A_r = A_{bubble}/A_{bottom}$, which depends on the phase distribution in microstructure.
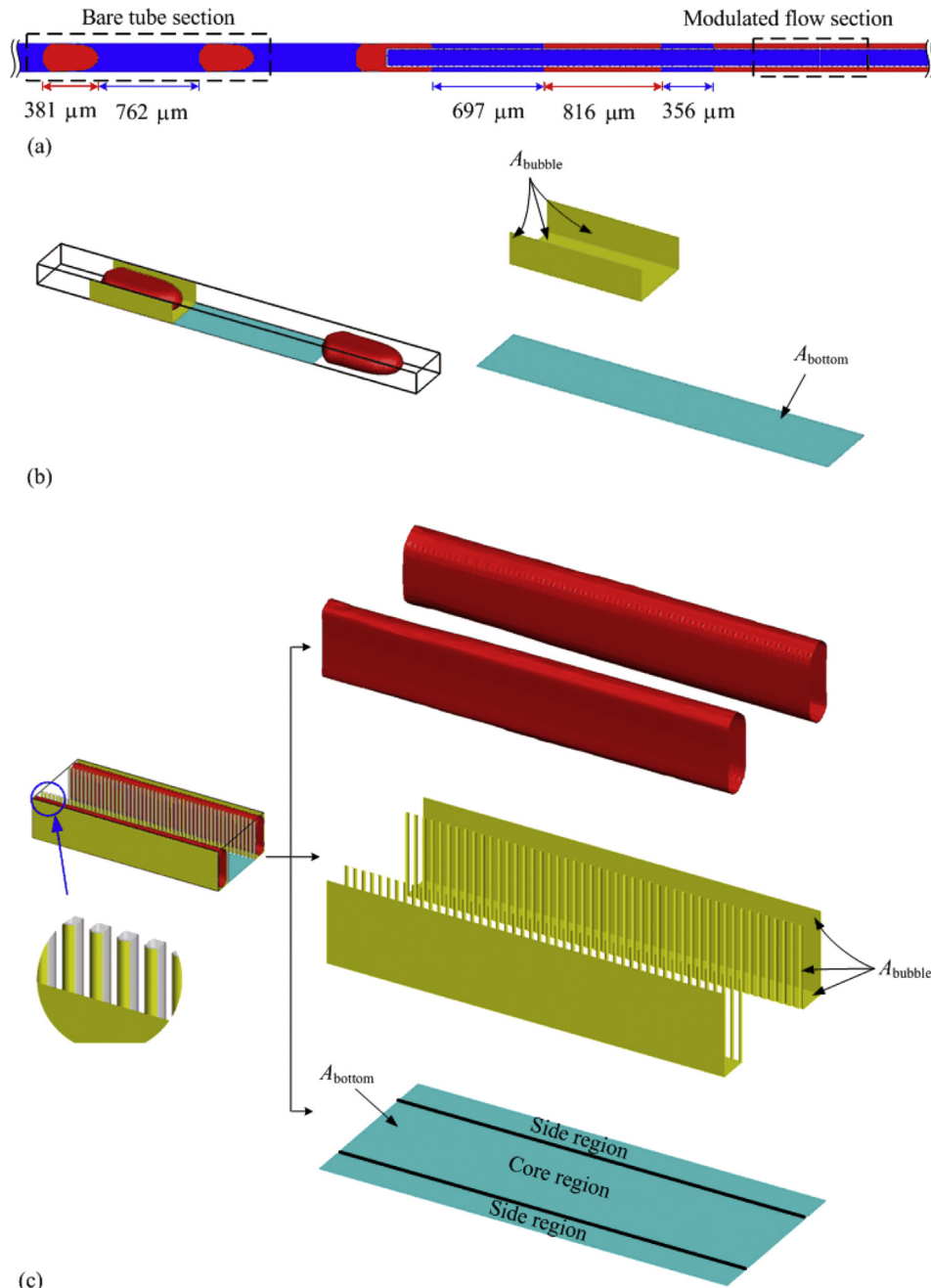

Fig. 10. Phase distribution (a), a slug bubble unit in the bare duct section (b), and bubble project area and bottom surface area in the fully phase separation section (c).

$$\frac{\dot{M}}{A_{bottom}} = \frac{\lambda_l(T_{sat} - T_w)}{h_{lg}} \frac{A_r}{\delta_a} \tag{25}$$

The heat transfer enhancement ratio k was defined to quantify the condensation rate in the fully phase separation section relative to that in the bare duct section as

$$k = \left(\frac{A_r}{\delta_a}\right)_M \bigg/ \left(\frac{A_r}{\delta_a}\right)_B \tag{26}$$

Equation (26) shows that the heat transfer enhancement ratio is related to the parameters of A_r and δ_a, in which A_r represents the bubble project area on which condensation heat transfer takes place relative to the channel bottom surface area, and δ_a depends on the bubble shape and local liquid film thickness. Table 4 shows these parameters for the three cases shown in Tables 2 and 3. It was found that A_r in the fully phase separation section was about two times of that in the bare duct section, majorly caused by the micro-membrane (pin-fin) effect. Introducing pin-fins significantly increased the vapor phase shadow area on solid walls. Besides, the averaged liquid film thickness was several times less in the fully phase separation section in contrast to the bare duct section. Finally, the heat transfer enhancement ratio, k, was varied from 7.0 to 11.4. That is to say, a properly designed phase separator could enhance the condensation heat transfer by ten times when it was used as a condenser. Fig. 11 shows the significantly decreased liquid film thickness in the fully phase separation section compared with those in the bare duct section, noting that the vertical coordinate used the logarithm coordinate.

6. Conclusions

The fast developed microsystem technology requires the phase separation in microchannel networks. A phase separator was proposed using the micro-membrane (pin-fin) structure. A straight microchannel was used with an enclosed micro-membrane populated at the microchannel center. The outlet was open to discharge the separated phases. When intermittent flow interacted with the micro-membrane, the increased surface energy prevented the gas phase from entering the micro-membrane inside. The simulation used the Volume of Fluid (VOF) method to track the gas–liquid interface. The results matched the experimental data regarding the bubble shape and liquid film thicknesses when the Taylor bubble

flowed in a square microchannel. A multiscale numerical simulation was performed to verify the fresh idea.

The phase separation process was discussed in detail. The separator consisted of a phase separating section and a fully phase separation section. Within the separating section, the two side regions contained confined bubble train flow. The liquid plugs were gradually shortened along the flow direction, caused by the liquid flowing towards the micro-membrane inside. When the velocity was referenced with the bubble velocity, liquid circulations were observed within the liquid plugs. The gas–liquid could be fully separated. Within the fully phase separation section, the liquid circulation was stopped. The gas was flowing in the side regions, with ultra-thin liquid films on the solid walls.

The proposed separator had the potential to be used as a condenser, where the condensation heat transfer should be enhanced. The heat transfer enhancement is related to A_r (the bubble project area relative to the bottom surface area) and an averaged liquid film thickness. In contrast to the bare duct section, the fully phase separation section significantly increased A_r and decreased liquid film thicknesses. The comprehensive heat transfer enhancement ratios could reach ten covering the present data range.

References

[1] L.E. Wiesegger, R.P. Knauss, G.E. Guntchnig, J.J. Brandner, R.J. Marr, Vapor-liquid phase separation in micro-/ministructured devices, Chem. Eng. Sci. 93 (2013) 32–46.
[2] R. Gupta, D.F. Fletcher, B.S. Haynes, Taylor flow in microchannel: a review of experimental and computational work, J. Comput. Multi 2 (2010) 1–31.
[3] A. Günther, K.F. Jensen, Multiphase micro fluidics: from flow characteristics to chemical and materials synthesis, Lab. Chip 6 (2006) 1487–1503.
[4] A. Günther, S.A. Khan, M. Thalmann, F. Trachsel, M.A. Schmidt, K.F. Jensen, Transport and reaction in microscale segmented gas–liquid flow, Lab. Chip 4 (2004) 246–278.
[5] A. Günther, M. Jhunjhunwala, M. Thalmann, M.A. Schmidt, K.F. Jensen, Micromixing of miscible liquids in segmented gas–liquid flow, Langmuir 21 (2005) 1547–1555.
[6] A. Hibara, S. Iwayama, S. Matsuoka, M. Ueno, Y. Kikutani, M. Tokeshi, T. Kitamori, Surface modification method of microchannels for gas–liquid two phase flows in microchips, Anal. Chem. 77 (2005) 943–947.
[7] C.C. Hsieh, S.C. Yao, Development of a microscale passive gas–liquid separation system, in: Proceedings of the 5th International Conference on Multiphase Flow, 2004. Yokohama, Japan.
[8] N. Assmann, P. Rudolf von Rohr, Extraction in microreactors: intensification by adding an inert gas phase, Chem. Eng. Process 50 (2011) 822–827.
[9] N. Kockmann, S. Dreher, M. Engler, P. Woias, Aerosol generation and handling in microchannels, Chem. Eng. J. 135 (2008) 121–125.
[10] C. Adiche, K. Sundmacher, Experimental investigation on a membrane distillation based micro-separator, Chem. Eng. Process 49 (2010) 425–434.
[11] M. Kraus, U. Krewer, Experimental analysis of the separation efficiency of an orientation independent gas/liquid membrane separator, Sep. Purif. Technol. 81 (2011) 347–356.
[12] F. Zenith, M. Kraus, U. Krewer, Model-based analysis of micro-separators for portable direct methanol fuel-cell systems, Comput. Chem. Eng. 38 (2012) 64–73.
[13] M.P. David, J. Miler, J.E. Steinbrenner, Y. Yang, M. Touzelbaev, K.E. Goodson, Hydraulic and thermal characteristics of a vapor venting two-phase microchannel heat exchanger, Int. J. Heat. Mass Transf. 54 (2011) 5504–5516.
[14] H.X. Chen, J.L. Xu, Z.J. Li, F. Xing, J. Xie, W. Wang, W. Zhang, Flow pattern modulation in a horizontal tube by the phase separation concept, Int. J. Multiph. Flow. 45 (2012) 12–23.
[15] Q.C. Chen, J.L. Xu, D.L. Sun, Numerical simulation of the modulated flow pattern for vertical upflows by the phase separation concept, Int. J. Multiph. Flow. 56 (2013) 105–118.
[16] J.H. Tsai, L.W. Lin, Active micro-fluidic mixer and gas bubble filter driven by thermal bubble micro-pump, Sens. Actuators A 97-98 (2002) 665–671.
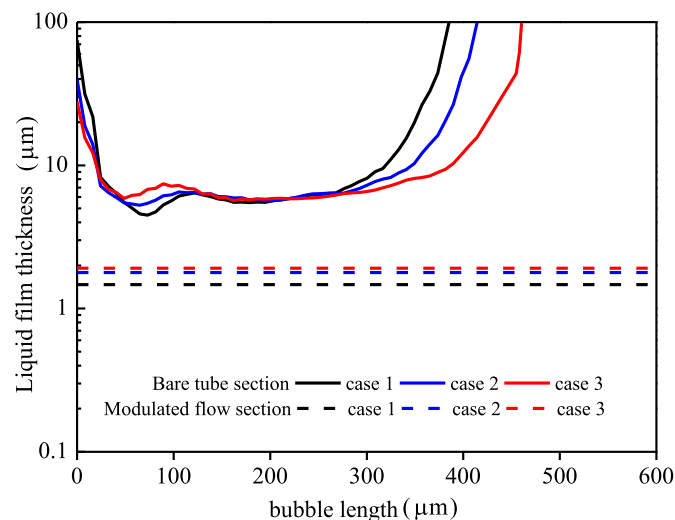
Fig. 11. Liquid film thicknesses in the bare duct section and fully phase separation flow section.

[17] J.U. Brackbill, D.B. Kothe, C. Zemach, A continuum method for modeling surface tension, J. Chem. Phys. 100 (1992) 335—354.

[18] A. Mehdizadeh, S.A. Sherif, W.E. Lear, Numerical simulation of thermofluid characteristics of two-phase slug flow in microchannels, Int. J. Heat. Mass Transf. 54 (2011) 3457—3465.

[19] A.L. Hazel, M. Heil, The steady propagation of a semi-infinite bubble into a tube of elliptical or rectangular cross-section, J. Fluid Mech. 470 (2002) 91—114.

[20] N. Shikazono, Y. Han, Two Phase Flow, Phase Change and Numerical Modeling, InTech, 2011 (Chapter 15).

[21] T. Taha, Z.F. Cui, CFD modeling of slug flow inside square capillaries, Chem. Eng. Sci. 61 (2006) 665—675.

[22] Y.S. Muzychka, E.J. Walsh, P. Walsh, Heat transfer enhancement using laminar gas-liquid segmented plug flows, J. Heat. Transf. 133 (2011) 041902.